Influence of Doppler broadening model accuracy in Compton camera list-mode MLEM reconstruction

Yuemeng Feng, Jean Michel Létang, David Sarrut, Voichita Maxim

To cite this version:

Yuemeng Feng, Jean Michel Létang, David Sarrut, Voichita Maxim. Influence of Doppler broadening model accuracy in Compton camera list-mode MLEM reconstruction. Inverse Problems in Science and Engineering, 2021, 29 (13), pp.3509-3529. 10.1080/17415977.2021.2011863 . hal-03481082

HAL Id: hal-03481082
https://hal.science/hal-03481082v1

Influence of Doppler broadening model accuracy in Compton camera list-mode MLEM reconstruction

Yuemeng Feng, Jean Michel Létang, David Sarrut, Voichiţa Maxim*

Univ Lyon, INSA-Lyon, Université Claude Bernard Lyon 1, CNRS, Inserm, CREATIS UMR 5220, U1294, F69621, Villeurbanne, France
* is the corresponding author

E-mail: `yfeng16@mgh.harvard.edu`, `{jean.letang, david.sarrut, voichita.maxim}@creatis.insa-lyon.fr`

November 2021

Abstract. The Compton camera is a gamma ray imaging device expected to provide clinically relevant images in the SPECT applications where collimated cameras are sub-optimal. Its imaging performances depend not only on the design of the detection system but also on choices related to tomographic reconstruction. The aim of this work is to show that the accuracy in modeling the acquisition largely influences the quality of the images. For this purpose we restrict here to Doppler broadening models in conjunction with the list-mode maximum likelihood expectation maximization (LM-MLEM) algorithm. The study was carried out with Monte Carlo simulation. We show that the reconstructed point spread function is location-dependent when the model is not accurate, and the usual elongation artefacts well-known in Compton camera imaging will appear. The model we propose allows to reconstruct isolated point sources and more complex non-uniform sources with improved resolution even in the direction orthogonal to the camera.

1. Introduction

Using the Compton camera to detect γ rays was proposed during 1970's simultaneously for astronomical ([1]) and nuclear medicine ([2]) imaging applications. Its advantage over other devices such as the widely employed collimated cameras and the coded aperture is the large angle acceptance. To identify the direction of an incoming γ ray the camera makes use of a coincidence mechanism based on Compton scattering. More recently its application to ion-range monitoring in proton and hadron-therapy through prompt-gamma detection was proposed. The energies of the prompt-γ rays are in this case too large to cope with parallel-hole acquisition, unless hard collimation is employed ([3, 4]), and this complicates three-dimensional imaging and reduces the resolution.

Despite the evident interest that Compton cameras may have in nuclear medicine applications ([5, 6, 7, 3, 8, 9, 10]), in the medical world imaging of γ sources is still carried out with collimated cameras. Along with the more complicated design and the cost of the detection system, the image reconstruction is also an important obstacle in their development. The projection data are noisy realizations of weighted integrals of the intensity of the source on conical surfaces. The difficulty to define an adapted mathematical model and the increased dimension of the projection manifold compared to traditional modalities PET and SPECT leads to a more challenging image reconstruction.

A strong argument in favour of Compton cameras is the theoretical possibility they offer to produce a three-dimensional image of the source with a single camera, without the need to make it turn around the patient. However, in practice the quality of three-dimensional reconstructions is limited. The most common artefact, seen as inevitable, is the elongation of the source in the direction orthogonal to the camera. Its origin can be easily explained by the missing data. Indeed, for an infinite planar camera and for ideal data, the dataset is complete, even over-determined and the reconstruction should be perfect ([11, 12]). The smaller the camera, the less complete the dataset and the more visible reconstruction artefacts should be. While this argument holds for analytic reconstruction with specific filtered back-projection algorithms, it was noticed that iterative algorithms are more robust to missing data ([13, 14, 15]). To put it simply, an iterative algorithm will solve a linear system. If the system is over-determined, the solution may be found even if some equations are withdrawn, where missing projections are interpreted as zeroes by the analytic algorithm. However, if the camera is very small, the shape and orientation of the projection cone do not vary much from one event to another, producing an ill-conditioned system matrix leading to a high sensitivity to noise. Regularization will improve the conditioning of the problem but should not solve it in extreme situations. We tried to understand if missing data is the actual and single cause of the elongation artefacts and of spatial Point Spread Function (PSF) variability, at least for data exempt of measurement uncertainties.

In this study we only consider uncertainties on the measured energies produced by Doppler broadening. The Doppler effect is a phenomenon first presented by Christian Doppler in 1842. It describes the change of frequencies or wavelengths of a wave source in relation to a moving observer. Due to the distribution of velocities of particles, Doppler effect will cause the broadening of spectral lines. In the pioneering experimental work of Du Mond [16] the Doppler broadening was considered and measured for the distribution of Compton spectra line. The probability distribution for a γ-ray to scatter with given energy and angle off an electron from the n^{th} electronic shell of the atom is described by a double-differential cross section depending on the electron's pre-collision momentum [17]. There is a balance between Compton cross-section and Doppler broadening in the conception of Compton camera [18]. Materials with low Z elements such as silicon are often chosen for the scatterer in order to achieve both high Compton to photoelectric ratio and low Doppler broadening. Scatterers made of Ge, CZT and $LaBr_3$ might be employed at high energies to reach a larger efficiency of detection, but the Doppler broadening might be increased and the Compton to photoelectric ratio will be reduced. In [19] this phenomenon was accounted for in the image reconstruction process as an event-dependent Gaussian mixture calculated from physical laws. The numerical tests show that precise modeling reduces the shift-variance of the image domain PSF. Still, the PSF is obviously changing as one moves further from the detector, although with a relatively small step. The considered camera has small dimensions, so the above discussion about missing projections likely applies. What is still unclear from these numerical tests is whether an appropriate model could completely remove artefacts at least for a relatively large camera, where the artifacts caused by the limited field of view can be neglected.

Acquisition models have to consider two influences: the solid angle an elementary detector surface covers at the source and the broadening of the conical surface due to the measurement uncertainties ([20, 21]). The latter used to be written as a weighted convolution of the source intensity with some kernel. This kernel can be expressed by Dirac on the cone when the data is ideal ([22]), a Gaussian ([23, 24, 21]), a von Mises distribution ([25]) or a Lorentzian [26]. Gaussian mixtures were investigated in 2D ([27]) and in 3D ([19]) for modeling Doppler induced uncertainties.

Three-dimensional images of the source were reconstructed with the list-mode (LM) version of the maximum likelihood expectation maximization (MLEM) algorithm. When the projection operator is sharp, namely when the conical surface model is taken, MLEM iterations have to be stopped early to limit the noise in the image. But when uncertainties are considered in a smoothing operator the convergence is slowed down by the intrinsic deconvolution. In this case, the high frequencies are very difficult to recover. This allows to obtain smooth images and a kind of numerical convergence in few iterations ([28, 29]). Nevertheless, the objects will remain blurred as the sharp edges are long to recover. Regularization with sparsity-inducing priors, as the total variation semi-norm, allows to control the noise ([30, 31]). It also accelerates convergence by addition of high frequencies specifically along the edges of the objects. By convergence we understand here numerical convergence. In this work we use total variation regularization and the convergent TV-MAP-EM algorithm from [32] for the reconstruction of sources that are not point-like.

We should mention here that when the projection operator is not perfectly fit to the acquisition model, the resulting image is the convolution of the true image (the one that would be produced with the appropriate projection operator) with a spatially-variant PSF ([33, 34]). In practice, the situation is more complex. The convolution kernels are difficult to calculate and the deconvolution process introduces ring artefacts. Low statistics is a degrading factor in this context.

The paper is organised as follows. Section 2 introduces the simulation set-up and the reconstruction strategy. Some variants of the models for the calculation of the sensitivity and of the system matrix are discussed. Then the Gaussian mixture model we propose is presented in this section. Finally we describe the Monte-Carlo simulations required for the calculation of the parameters of the model and for the numerical tests. The fitted models are shown in section 3. Section 3 also shows some numerical results. They concern the spatial variability of the reconstructed point spread function and the reconstruction of a non-symmetric source with variable intensity. Section 4 is dedicated to discussions on the methods and results and in section 5 we present our conclusions.

2. Materials and methods

2.1. The Compton camera

A Compton camera is usually composed of at least one scattering detector and one absorption detector. A photon detected by the camera is recorded as a Compton coincidence when it satisfies the following conditions. First, the photon has to scatter on an electron from the detector, where it deposits parts of its energy. Then the scattered photon may undergo other interactions. Finally, it should be absorbed by photo-electric absorption. The unknown Compton scattering angle β_G can be estimated from the measured energies. It corresponds geometrically to the angle between the direction of the incident ray and the direction of the scattered ray. The estimated value is denoted hereafter β_E and can be calculated from the known initial energy E_0 and the energy deposited in the first interaction recorded as E_1 following the equation:

$$\cos(\beta_E) = 1 + \frac{m_e c^2 E_1}{(E_0 - E_1)E_0}, \tag{1}$$

where m_e denotes the rest mass of an electron and c denotes the speed of light. When the initial energy is unknown, its value can be estimated as the sum of energies deposited by the photon. With the position of the first and second interactions being recorded as V_1 and V_2, it can be deduced that the photon was emitted somewhere on the surface of the cone $\mathscr{C}(V_1, V_2, \beta_E)$ with apex V_1, axis direction $\overrightarrow{V_2V_1}$ and half-opening angle β_E. Figure 1 illustrates the geometry of the camera used in our study. The camera is composed of three stripped silicon scatterers (512 strips on each face) and a segmented $LaBr_3$ (lanthanum bromide) absorber with individual crystals of $0.5 \times 0.5 \times 4$ cm^3. The thickness is 0.2 cm for the scattering layer.

We do not consider here the events with three or more Compton interactions, which do not require the knowledge of the initial energy E_0, but might be more sensitive to noise ([35, 36]). In practice the recorded energy E_1 is usually associated with some uncertainties due to the limited energy resolution of the detectors. This causes inexact measurement of the energy deposited by the electron ejected from the nuclear shell by the scattered γ ray. Besides, the deposited energy is also affected by Doppler broadening, related to the fact that the electron is in motion. Even for ideal detectors capable to measure exactly the energy of the scattered electron, the Doppler broadening means that the measured deposited energy E_1 will not lead to the real scattering angle β_G. The energy uncertainties produce angular uncertainties known under the name of angular resolution measurement (ARM). The theoretical conical surface becomes a conical shell. The thickness and the internal consistency of the shell depend on the model of uncertainties.

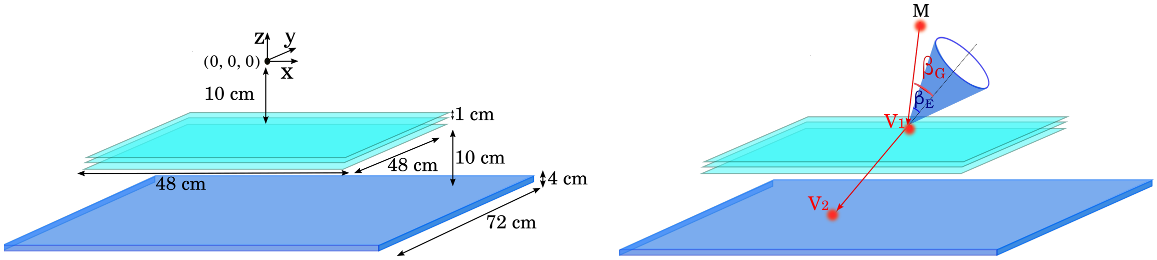

(a) (b)

Figure 1. (a) Illustration of the simulation geometry. The camera is composed of three scatterers and an absorber with large surfaces. (b) Acquisition parameters. A photon emitted at a point M will undergo Compton scattering at some point V_1 from the scatterer then will be absorbed at V_2. The unknown Compton angle β_G can be estimated form the measured energies. The estimated value is denoted β_E. The point M that should in theory lie on the conical surface will belong in practice to a conical shell defined by the measurement uncertainties.

2.2. *Image reconstruction*

The number of photons detected by virtual elements of Compton camera follows Poisson laws. Let Y denote the vector of measurements and λ denote the mean vector of photons emitted by the J voxels. The reconstruction algorithm MLEM ([37, 38]) solves the minimization problem:

$$\min\{-\ell(\lambda|Y)\ :\ \lambda\in(\mathbb{R}_+)^J\},\tag{2}$$

where the log-likelihood function is defined as:

$$\ell(\lambda|Y)=\sum_{i=1}^{I}\left(-\sum_{j=1}^{J}t_{ij}\lambda_j+y_i\ln(\sum_{j=1}^{J}t_{ij}\lambda_j)-\ln(y_i!)\right),\tag{3}$$

where I is the total number of data bins. For list-mode data, no more than one event can be detected in a given bin. We thus have $y_i=1$ if an event was detected in the bin and $y_i=0$ otherwise. The list mode is particularly well adapted for Compton camera imaging where the number of detected events is extremely low with respect to the dimension of the data space. We denote hereafter $\mathcal{I}$ the index set of the detected events. Let t_{ij} denote the probability of a photon emitted in voxel j to be detected as event i. The matrix T composed of these probabilities is the matrix of the system. The LM-MLEM reconstruction algorithm consists in calculating, starting from some initial value $\widehat{\lambda}^0\in(\mathbb{R}_+^*)^J$, the sequence

$$\widehat{\lambda}_j^{l+1}=\frac{\widehat{\lambda}_j^l}{s_j}\sum_{i\in\mathcal{I}}\frac{t_{ij}}{\sum_k t_{ik}\widehat{\lambda}_k^l},\tag{4}$$

where $s=(s_j)_{j=1,\ldots,J}$ is the so-called sensitivity vector, containing the detection probabilities for photons emitted from voxels. Equation (4) can be reformulated using matrix multiplication and element-wise operations on vectors as:

$$\widehat{\lambda}^{l+1} = \frac{\widehat{\lambda}^l}{s} T^* \left[\frac{\mathbf{1}}{T\widehat{\lambda}^l} \right], \tag{5}$$

where T^* is the adjoint operator of T and corresponds to back-projection and $\mathbf{1}$ is a vector of ones with the same size as the projection. The images produced by the MLEM algorithm are very noisy. For sources that are not point-like, the iterations have to be stopped before high frequencies are added and the resulting images have to be smoothed. On the purpose of reducing the noise caused by Poisson-distributed data in the extended source, we have applied a total-variation regularized reconstruction which consists to solve:

$$\min\{-\ell(\lambda|Y) + \alpha\|\lambda\|_{TV} \,:\, \lambda \in (\mathbb{R}_+)^J\}, \tag{6}$$

where $\|\cdot\|_{TV}$ is the TV semi-norm and α is a strictly positive regularization parameter. The discrete total variation of λ seen as a three-dimensional image, element of $\Lambda = \mathbb{R}^{J_x \times J_y \times J_z}$ with $J_x J_y J_z = J$, is defined as:

$$\|\lambda\|_{TV} = \sum_{1 \le i \le J_x, 1 \le j \le J_y, 1 \le k \le J_z} |(\nabla\lambda)_{i,j,k}|, \tag{7}$$

where $(\nabla\lambda)_{i,j,k}$ is the discrete gradient of the image at voxel (i, j, k) and $|v| = \sqrt{v_1^2 + v_2^2 + v_3^2}$ is the norm of the three-dimensional vector $v = (v_1, v_2, v_3) \in \mathbb{R}^3$. Let us consider $\Gamma = \Lambda \times \Lambda \times \Lambda$ the space of gradients with its scalar product:

$$\langle p, q\rangle_\Gamma = \sum_{i,j,k} (p^1_{i,j,k} q^1_{i,j,k} + p^2_{i,j,k} q^2_{i,j,k} + p^3_{i,j,k} q^3_{i,j,k}), \quad \text{for all } (p, q) \in \Gamma \times \Gamma. \tag{8}$$

An equivalent definition of $\|\lambda\|_{TV}$ is then:

$$\|\lambda\|_{TV} = \sup\left\{\langle\varphi, \nabla\lambda\rangle_\Gamma \,:\, \varphi \in \Gamma \text{ such that } |\varphi_{i,j,k}| \le 1,\ 1 \le i \le J_x, 1 \le j \le J_y, 1 \le k \le J_z\right\}. \tag{9}$$

We applied here the MAP-EM algorithm from [32], consisting to alternate LM-MLEM steps

$$\widehat{\lambda}_j^{l+1/2} = \frac{\widehat{\lambda}_j^l}{s_j} \sum_{i \in \mathcal{I}} \frac{t_{ij}}{\sum_k t_{ik} \widehat{\lambda}_k^l}, \tag{10}$$

with Poisson TV-denoising in a globally convergent algorithm. The denoising step consists to solve the minimization problem:

$$\widehat{\lambda}^{l+1} \in \operatorname*{arg\,min}_{u \in (\mathbb{R}_+)^J} \left\{ \langle u - \widehat{\lambda}^{l+1/2} \log u, s\rangle + \alpha\|u\|_{TV} \right\}, \tag{11}$$

which is a weighted Poisson denoising. The solution writes:

$$\widehat{\lambda}^{l+1} = \frac{s\widehat{\lambda}^{l+1/2}}{s + \alpha \operatorname{div}\varphi^*}, \tag{12}$$

where $\varphi^* \in \Gamma$ is the limit of the sequence defined as $\varphi^0 = 0 \in \Gamma$ and

$$\varphi^{k+1} = \frac{\varphi^k - \tau p^k}{1 + \tau |p^k|}, \text{ with } p^k = \nabla \left(\frac{s \widehat{\lambda}^{l+1/2}}{s + \alpha \mathrm{div} \varphi^k} \right). \tag{13}$$

Arithmetical operations on vectors are applied element-wise and div is the divergence operator. The minimization step τ should be chosen such that $\tau < \alpha/L$, where

$$L = 12\alpha^2 \frac{\|s\widehat{\lambda}^{l+1/2}\|_\infty}{(s_{\min} - 6\alpha)^2}, \tag{14}$$

is a function of the sensitivity s, of its minimum value $s_{\min} = \min_j s_j$, of the image to be denoised $\widehat{\lambda}^{l+1/2}$ and of the regularization parameter α. Note that the regularization parameter has to verify the constraint $\alpha < s_{\min}/6$.

2.3. Sensitivity

We evaluate separately sensitivity and system matrix, both by analytic models. In theory the sensitivity should be calculated as $s_j = \sum_i t_{ij} = (T^*\mathbf{1})_j$ with the sum taken on all possible events. However, in the evaluation of the system matrix described hereafter we neglect some coefficients which depend only on the event and thus get cancelled in the reconstruction formula (4). These coefficients are probabilities difficult to estimate precisely. Numerical errors on these coefficients would not affect the reconstruction but are important if we want to calculate the sensitivity as $s = T^*\mathbf{1}$. The mismatch between sensitivity and system matrix might be a source of artefacts in the reconstruction.

We consider a coordinate system with the z axis perpendicular to the camera and passing through its center (see figure 1). Each of the L scatterer layers has dimensions $(2a, 2b, d)$ cm. As shown in figure 2, we denote $O_j(x_j, y_j, z_j)$ the center of voxel j, $D_{j,n}$ the distance from O_j to the n^{th} scatterer and θ_j the angle made by a vector $\overrightarrow{NO}_j$, N from the scatterer, with the z axis.

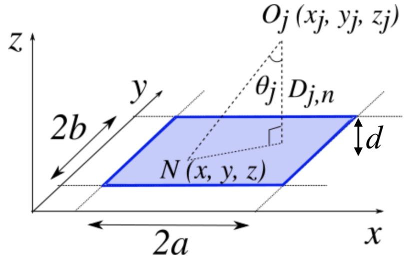

Figure 2. Sensitivity calculation for the j^{th} voxel. The point $O_j(x_j, y_j, z_j)$ is the center of voxel j, $D_{j,n}$ is the distance from O_j to the n^{th} scatterer and $(2a, 2b, d)$ are dimensions of a scatterer layer.

Assuming that the probability of generating a Compton event is the same for all the photons once they have been scattered, we calculate hereafter the sensitivity with the model M1:

$$s_j \propto \sum_{n=1}^{L} \int_{-a}^{a} \int_{-b}^{b} \frac{\cos\theta_j}{(x-x_j)^2+(y-y_j)^2+D_{j,n}^2} \left(1-e^{-\mu_c d/\cos\theta_j}\right) e^{-(n-1)\mu_t d/\cos\theta_j} dydx, \quad (15)$$

with L the number of layers. The first factor accounts for the solid angle of the detector pixel seen from the center of the voxel, the second accounts for the probability of interaction in the n^{th} scattering layer and the last one accounts for the probability that the photon pass through the $n-1$ previous layers without interaction. The linear attenuation coefficients μ_c and μ_t stand respectively for Compton and total attenuation. They depend on detector material and photon energy. The calculation can be deduced from the data table in [39]. For 511 keV gamma rays in Silicon (density 2.32), the Compton linear attenuation coefficient is $\mu_c = 0.199\text{cm}^{-1}$ and the total linear attenuation coefficient $\mu_t = 0.201\text{cm}^{-1}$.

The numerical evaluation of (15) is relatively time consuming (order of minutes) but can be calculated once and saved for further use. If the attenuation factors are neglected one obtains the model from [27]. When the value of $\mu_c d/\cos\theta_j$ is close to zero, the factor $1-e^{-\mu_c d/\cos\theta_j}$ can be replaced with its first order approximation leading to sensitivity model:

$$s_j^{M1} \propto \sum_{n=1}^{L} \int_{-a}^{a} \int_{-b}^{b} \frac{1}{(x-x_j)^2+(y-y_j)^2+D_{j,n}^2} e^{-(n-1)\mu_t d/\cos\theta_j} dydx. \quad (16)$$

If we further neglect the variability of the absorption probability in the previous layers we obtain the model M2, given as:

$$s_j^{M2} \propto \sum_{n=1}^{L} \int_{-a}^{a} \int_{-b}^{b} \frac{1}{(x-x_j)^2+(y-y_j)^2+D_{j,n}^2} dydx, \quad (17)$$

that can be partially evaluated as:

$$\begin{aligned} s_j^{M2} \propto \ & \sum_{n=1}^{L} \int_{-a}^{a} \frac{1}{(x-x_j)^2+D_{j,n}^2} \left(\arctan\left(\frac{b-y_j}{\sqrt{(x-x_j)^2+D_{j,n}^2}}\right)\right. \\ & \left. + \arctan\left(\frac{b+y_j}{\sqrt{(x-x_j)^2+D_{j,n}^2}}\right)\right) dydx. \end{aligned} \quad (18)$$

The performances of these two models can be appreciated in figure 3 where they are compared to Monte-Carlo simulation from point sources emitting at 511 keV. The sources were placed at different positions on (a) a line parallel to the Ox axis at 4 cm for the upper scatterer and (b) on the Oz axis. Only Doppler broadening was simulated as data degradation factor. We obtained qualitatively the same results for realistic data (not shown

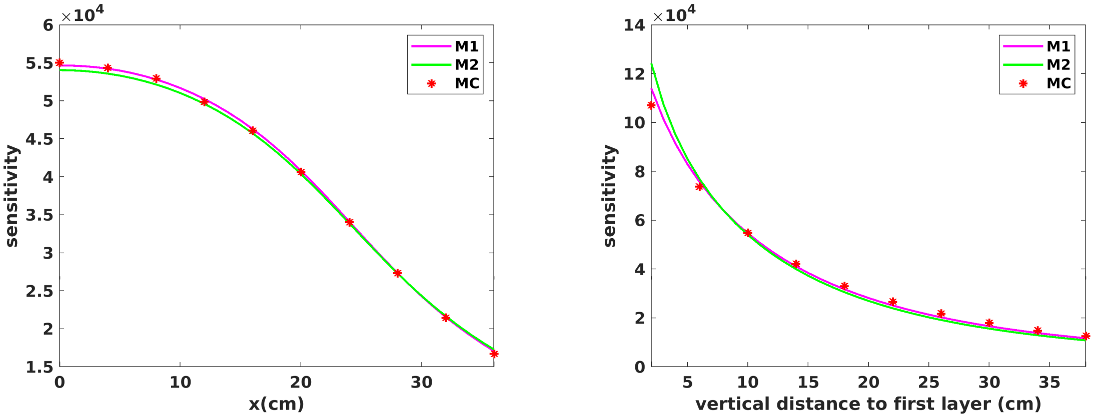

(a) (b)

Figure 3. Comparison of the models M1-M2 against Monte-Carlo simulations (see text for details).

here), where we considered not only the Doppler broadening, but also the limited spatial and energy resolution as the source of the uncertainties.

The numerical computation was implemented on Intel Core i7-6600U CPU @ 2.60GHz as a rectangle integration scheme with 100 equispaced sampling points in each dimension. For a volume with $41 \times 41 \times 41$ voxels the calculation of sensitivity by M1 takes about 400 seconds, while M2 takes only two seconds. The model M1 performs reasonably well against simulation. Model M2 is hundreds times faster to compute but shows more discrepancies with the simulation. For this reasons we will use hereafter the model M1.

2.4. Doppler broadening modeling in the system matrix

An approximate value of the sensitivity can be calculated with a large Monte Carlo simulation. Calculation of the system matrix by Monte Carlo simulation is a challenging task because of the large dimension of the data space. Rough approximations and binning would be necessary.

The coefficient t_{ij} of the system matrix T is calculated with the equation from [20]. Some other models have been proposed in the literature ([25, 23, 40, 9]). For an event i where the Compton scattering with some measured angle β_E occurs at V_1 and the absorption at V_2 and for a voxel j we use a quadrature formula with a single node to approximate the integral:

$$t_{ij} = \int_{P \in v_j} K(\beta_G, E_0) \frac{\cos \theta_{\overrightarrow{V_1 P}}}{|\overrightarrow{V_1 P}|^2} h(\delta|\beta_E) dv \,, \tag{19}$$

where β_G is the geometric angle between the vectors $\overrightarrow{V_1 P}$ and $\overrightarrow{V_1 V_2}$ (see figure 1), $K(\beta, E_0)$ is the Klein-Nishina differential cross section of Compton scattering with angle β at some given initial energy E_0, and the next factor represents a solid angle. The angular distance from $\overrightarrow{V_1 P}$ to the cone is $\delta = \beta_G - \beta_E$ and $h(\cdot|\beta_E)$ is a kernel modeling the uncertainties on the Compton angle. In our study it only accounts for Doppler broadening. Involving this effect in analytical methods allows to improve the quality of reconstruction ([41]).

For the purpose of the comparison we also simulated Doppler-free ideal data. The images were then reconstructed with a variant of (19) where $h(\cdot|\beta_E)$ was replaced with a narrow Gaussian function with argument the Euclidean distance from the center of the voxel j to the conical surface of event i. When the standard-deviation parameter decreases to zero, we obtain an approximate value for the conical surface integral. In our algorithm we fixed the value of the standard deviation to one voxel and we cut the Gaussian to 3σ. Another way to calculate the surface of the intersection between the cone and the voxel is to use a ray-tracing algorithm and the appropriate quadrature formula. We found this method more time consuming as a large number of rays should be traced for a complete sampling of the volume ([42]).

The shape of the ARM distribution that translates energy uncertainties in angular uncertainties has a narrow peak and long tails. In [25] authors proposed a von Mises fit of the ARM. For narrow distributions, the von Mises distribution can be approximated with a Gaussian. The Voigt function, which is a convolution of the Gaussian distribution and the Lorentzian distribution, was used to fit ARM distributions with long tails in [26]. Uncertainties caused by Doppler broadening are often modeled by a Gaussian kernel ([40, 9]) or neglected against uncertainties from realistic data also modeled with Gaussians ([18, 43, 20]). In reality, different contributions from the different electronic orbitals build up and produce this distribution. In order to approximate the long tails, in [19] a mixed Gaussian model was considered. Also, an accurate error distribution model specific to Germanium detectors was developed.

For a point source at some known position denoted M, the exact scattering and absorption positions were obtained from the simulation. The true (geometrical) scattering angle can then be computed from a scalar product:

$$\cos(\beta_G) = \frac{\overrightarrow{MV_1}.\overrightarrow{V_1V_2}}{|\overrightarrow{MV_1}||\overrightarrow{V_1V_2}|}. \tag{20}$$

The angular uncertainties are measured by the ARM, calculated for each event as $\delta = \beta_G - \beta_E$. We fitted both a Gaussian and a mixture of Gaussian distributions to the empirical ARM histogram. Because of the similarity between von Mises and Gaussian distribution, we didn't apply the von Mises fit. The Gaussian fit consists to evaluate the parameters k and σ that minimize the ℓ_2 error between the empirical distribution and the model

$$h(\delta; k, \sigma) = k \exp\left(-\frac{\delta^2}{2\sigma^2}\right). \tag{21}$$

The Gaussian mixture fit consists to evaluate the parameters k_1, σ_1 and k_2, σ_2 that minimize the ℓ_2 error between the empirical distribution and the model

$$h(\delta; k_1, \sigma_1, k_2, \sigma_2) = k_1 \exp\left(-\frac{\delta^2}{2\sigma_1^2}\right) + k_2 \exp\left(-\frac{\delta^2}{2\sigma_2^2}\right). \tag{22}$$

We also tested mixtures of more than two Gaussians. As the images we obtained were very close to the ones provided by the simpler two-Gaussian mixture model in the case of Silicon, we do not show them here.

2.5. Data simulation

The Monte Carlo simulation were performed with the Gate toolkit, version 8.2 [44] and Geant4 version 10.5. We have alternatively selected the physics model in order to account or not for the Doppler effect. The events with only two interactions, one Compton scattering and one photo-electric process, are selected and their ordering is known. The positions of the hits and the deposited energies are exactly measured by the detector. The electron generated in the Compton interaction is not tracked in the simulation. We took *option 1* of the standard electromagnetic physics list for ideal data without Doppler broadening caused uncertainties, and *option 4* for data simulated with Doppler broadening. The Compton scattering in *option 4* is implemented by the Monash University model [45] which uses a relativistic formalism and the conservation of energy and momentum to derive the energy and angular distributions of Compton scattered photons off non-stationary atomic bound electrons. Four point sources were simulated for the calculation of the ARM, one emitting at 4 MeV and three emitting at 511 keV. The source emitting at 4 MeV is placed in $(0, 0, 0)$ in centimeters. The sources emitting at the lower energy are placed at different distances from the camera and from its axis in order to evaluate the relation between ARM and source position. Their positions are respectively $(0, 0, 0)$, $(0, 0, -5)$ and $(20, 20, 0)$ in centimeters.

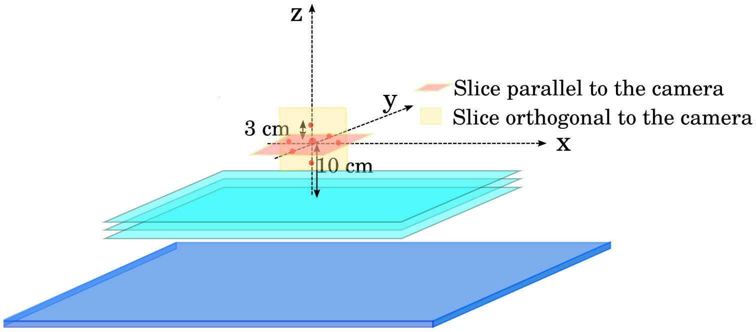

Figure 4. Geometry of simulation for the source composed of seven points.

To evaluate the influence of the proposed Gaussian mixture model on the images, we calculated the reconstructed PSF at different positions. We simulated seven mono-energetic point sources emitting simultaneously at 511 keV, located at (0, 0, 0), (0, 0, 3), (0, 0, -3), (0, 3, 0), (0, -3, 0), (3, 0, 0), (-3, 0, 0) in centimeters. 20,000 Compton events are used for the reconstruction. The simulation geometry is depicted in figure 4, along with two planes that indicate the positions of the slices extracted for visualisation from the reconstructed volume.

We then simulated a mono-energetic source consisting of five letters with thickness 1 cm centered on the origin, 10 cm away from the detector. The intensity was piece-wise

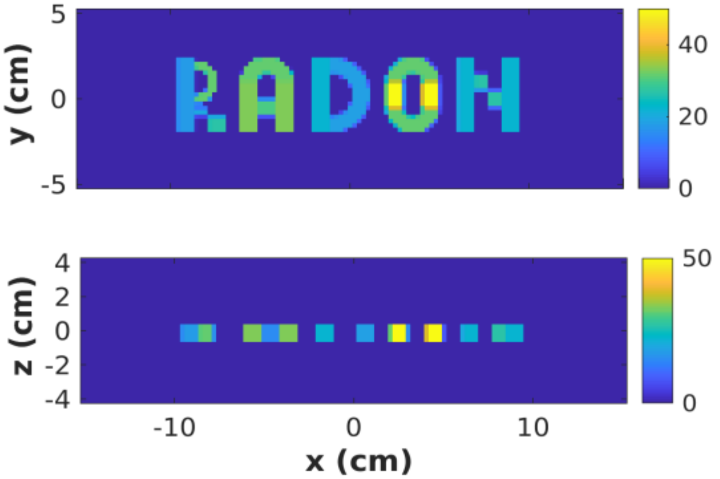

Figure 5. Central slices from the mono-energetic non-uniform source.

constant and the γ photons were emitted at 511 keV. The letters were placed first parallel then perpendicular to the camera, in order to observe the elongation in the axial direction. Central slices of the source are shown in figure 5. For each test we simulated 2×10^5 Compton events.

3. Results

3.1. Fit of the angular resolution measurement

The uncertainties caused by Doppler broadening depend on the material and the initial energy of photons. In figure 6 is shown the distribution of the Doppler-modified Compton angle β_E as function of its true value β_G, for a first interaction in the scatterer in (a) and a first interaction in the absorber in (b). In other words, the two sub-figures show respectively the dispersion for silicon and lanthanum bromide at 511 keV.

The colors in the figure are related to the number of counts. Over 60% simulated photons will not produce an event. A number of 3×10^7 photons were simulated to obtain 4×10^5 Compton events, 30% of events will interact twice on the same layer. Only about 2% of events had a first interaction in the absorber. For the events with a first interaction on the scatterer layer, the maximum value of β_G is 147°. This value can be explained by the camera geometry depicted in figure 1 and corresponds to the photons being scattered on one boundary of the first scattering layer and then absorbed on the opposed boundary of the absorber.

Figure 7 shows the ARM distribution extracted from all two-sites events for four sources, one emitting at 4 MeV and the others emitting at 511 keV. The empirical distributions plotted with red dotted lines are histograms with 0.125° bins. Gaussian fits of the histograms were calculated following equations (21) and (22). They are plotted respectively as clear blue and

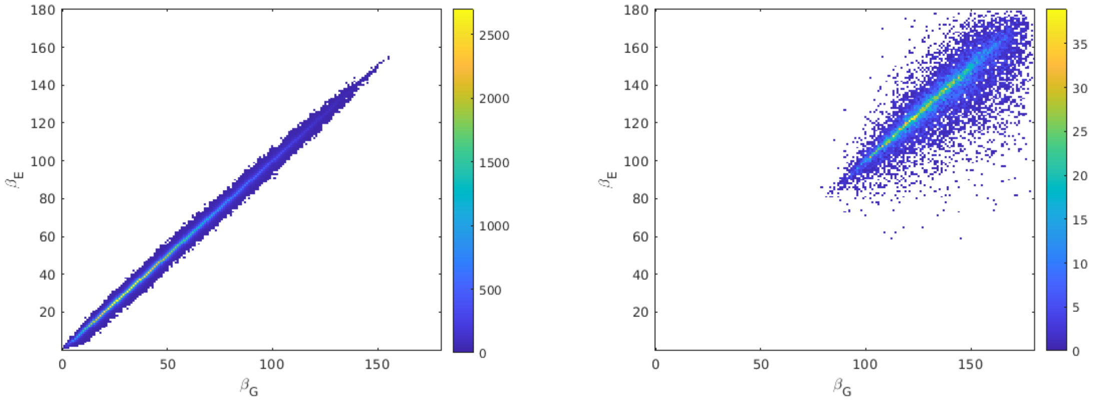

(a) First interaction occurs on the scatterers (b) First interaction occurs on the aborber

Figure 6. Uncertainties of Compton scattering angle for ideal data with Doppler broadening. The value β_E calculated from energies is plotted as function of the geometrical value β_G. (a) Events with first hit in the scattering detector. (b) Events with first hit in the absorber. Among the two-site events, 98% are in (a) and 2% are in (b). The uncertainty on the scatter angle depends on the uncertainties on the deposited energies. In our simulation the total energy being known, only uncertainties on the energy deposited in the scatterer are considered. Energy uncertainties are taken constant in Silicon and depend on the energy of the incident photon in $LaBr_3$. The distribution of β_E in (a) is less dependent on the scattering angle than in (b), although some variability persists due to equation (1).

the dark blue lines. The uncertainties increase when the energy decreases from 4 MeV to 511 keV, as it can be seen by comparing panels (a) and (b). From panels (b)-(d) it could be deduced that this averaged distribution is not very sensitive to the distance to the source.

Numerical results for the different sources and fits are shown in table 1. The Gaussian mixture model allows for a mean square error (MSE) two orders of magnitude lower compared to the Gaussian fit at 511 keV.

Table 1. Parameters of the Gaussian fit

case in Fig.7	single Gaussian			Gaussian mixture				
	(k, σ, MSE $\times 10^{-8}$)			(k_1, σ_1, k_2, σ_2, MSE $\times 10^{-8}$)				
a	0.0503	0.1346	242.80	0.0456	0.0621	0.0175	0.3490	11.59
b	0.0317	0.5438	151.64	0.0292	0.2350	0.0116	1.3424	2.16
c	0.0428	0.6097	200.58	0.0399	0.2497	0.0161	1.4675	3.37
d	0.0256	0.5699	117.42	0.0236	0.2335	0.0099	1.3215	2.40

3.2. Position dependency of the image PSF

We reconstructed the image of the source composed of seven mono-energetic point sources as a volume of size 10.25^3 cm^3 divided into 41^3 voxels. Each voxel measures 2.5^3 mm^3. We

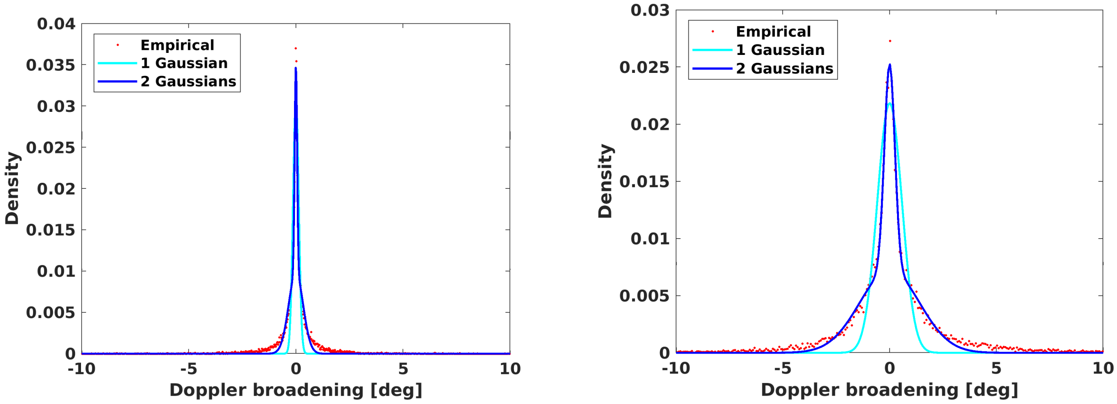

(a) 4 MeV, source in (0,0,0) cm, 10 cm to the camera, FWHM= 0.5°

(b) 511 keV, source in (0,0,0) cm, 10 cm to the camera, FWHM = 1°

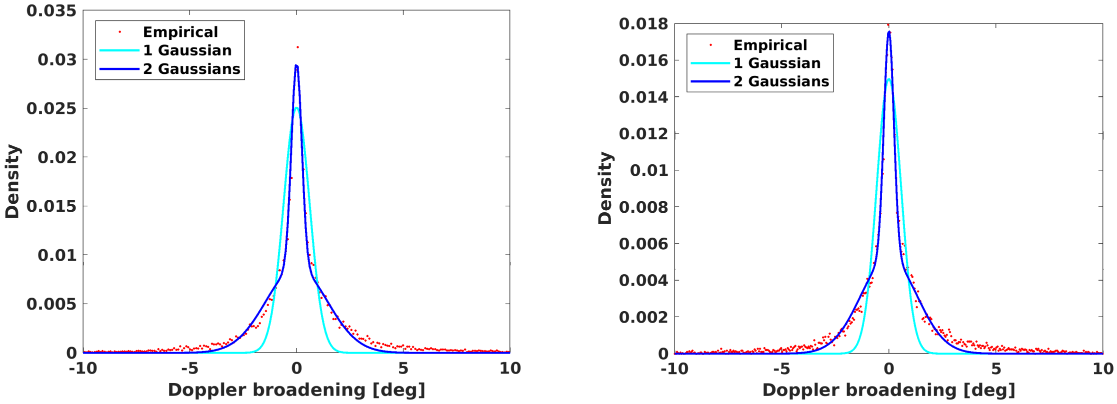

(c) 511 keV, source in (0,0,-5) cm, 5 cm to the camera, FWHM= 1°

(d) 511 keV, source in (20,20,0) cm, 10 cm to the camera, FWHM= 1°

Figure 7. Distribution of Doppler angular uncertainties. The errors on the Compton angle are calculated as $\beta_G - \beta_E$ and only for the two-site events with first interaction on the scattering layer. (a) Point source emitting at 4 MeV. (b)-(d) Point sources emitting at 511 keV at different positions as indicated in the captions. For each configuration the histogram of values is plotted as red dotted line and the FWHM is shown. The clear blue and the dark blue lines represent Gaussian fits with respectively one Gaussian and a linear combination of two Gaussians. Their parameters are shown in table 1

normalised the volumes to their maximum of intensity. Results are shown in figure 8. The algorithm began to converge after 20 iterations, as shown in figure 9(b) where the ℓ_2 distance between the iterates was plotted. For this reason we stopped the algorithm at 50 iterations.

In figure 8 we show results for simulations with and without Doppler broadening. The first column corresponds to the reconstruction of data simulated without Doppler broadening and reconstructed with the model described in section 2.4 for Doppler-free data. The second and third columns show data simulated with Doppler broadening. The second column shows the reconstruction with a single Gaussian kernel modeling the Doppler-induced uncertainties.

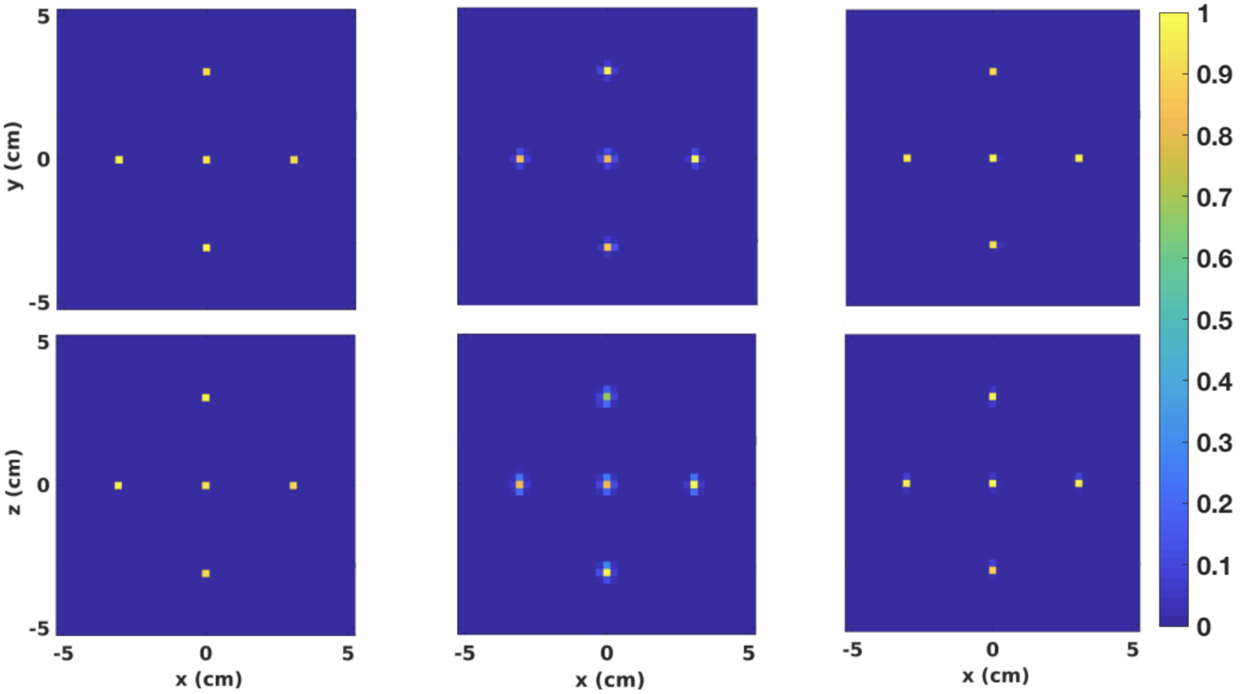

(a) ideal data (b) Gaussian ($\sigma = 0.54°$) (c) Gaussian mixture

Figure 8. Central slices in the planes xy (first line) and yz (second line) from the volume representing the source composed of seven mono-energetic point-like sources. The geometry of the simulation is represented in figure 4. The first column shows images for data simulated without Doppler broadening. The second and third column show the reconstruction of data simulated with Doppler broadening. For the second column we took the kernel h as a Gaussian with standard deviation $\sigma = 0.54°$, value extracted from table 1, single Gaussian fit, case (b). For the third column, h was taken as a Gaussian mixture with parameters given in table 1, case (c).

Its standard-deviation $\sigma = 0.54°$ is the one estimated from the Monte Carlo simulations and given in table 1 (b) for the single Gaussian fit. The third column is the reconstruction obtained with the Gaussian mixture parameters.

Figure 9(a) shows central profiles through the volumes in the direction orthogonal to the camera. The intensities of the sources are closer to each other when the Gaussian mixture model is used. The profile is moreover similar to the one obtained for the simulation without Doppler broadening.

Increasing the value of σ leads to smooth images, but to even more heterogeneous PSFs. This can be seen in figure 10 for $\sigma = 1.8°$, where obviously the intensities of the sources were not reconstructed to the same value.

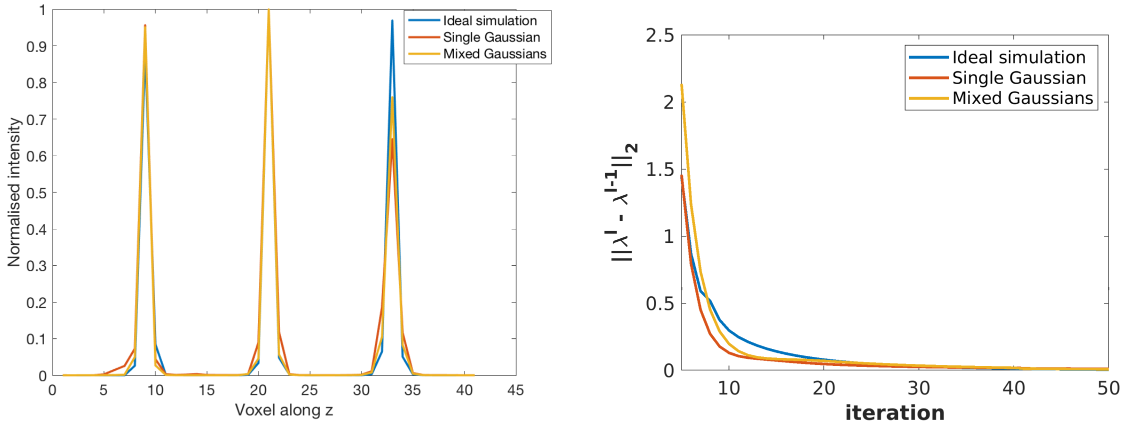

(a) Central profile from the reconstructed volume taken through the vertical direction.

(b) Difference between each iteration

Figure 9. (a) Central profile from the reconstructed volume taken through the vertical direction. (b) The LM-MLEM algorithm began to converge numerically after 20 iterations, but 50 iterations were performed to ensure that the images will not change significantly.

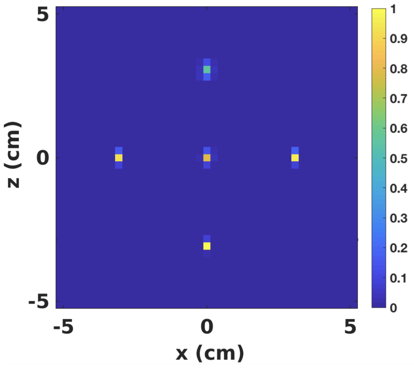

Figure 10. Typical PSF heterogeneity induced by inaccurate modeling of the ARM. A single Gaussian was used here with $\sigma = 1.8°$, two times larger than the one from figure 8.

3.3. Non-uniform source

We consider here the mono-energetic non-uniform source consisting of five letters, represented in figure 5. We ran 200 iterations of the TV-MAP-EM algorithm described in section 2.2, although numerical convergence was reached much earlier. The TV regularization parameter was set to 5×10^{-6} for all the experiments. Note that this value depends on the sensitivity vector which in our case is calculated to reproduce simulations up to a multiplicative constant that may be different from a model to another. The reconstructed volumes were composed of $121 \times 33 \times 41$ voxels of dimensions $0.25 \times 0.25 \times 0.25$ cm^3 each and we normalised the images to their maximum.

In figure 11 we show the central slices of the volume for the source placed parallel to the camera. In figure 12 we show central slices for the source placed perpendicular to the

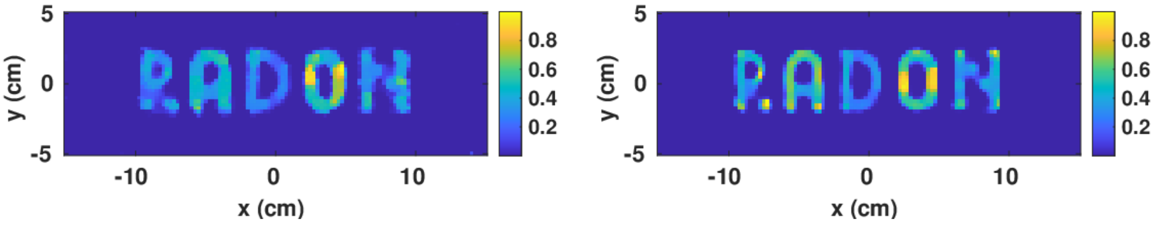

(a) with Doppler broadening (b) without Doppler broadening

Figure 11. Central slices of the reconstructed volume obtained for the non-uniform source when placed parallel to the camera. The physics model differ between the two images to include or not Doppler broadening. We used the reconstruction model adapted to each data type. Results are shown after 50 iterations of the TV-MAP-EM algorithm with regularization parameter $\alpha = 5 \times 10^{-6}$. The slices are normalised to their maximum.

camera: the two slices differ in the physics model that is used in the simulations (including or not Doppler broadening) but also in the way the acquisition is modeled in the system matrix. For the Doppler data we used the Gaussian mixture model. Figure 14 shows the mean square error (MSE) and the structural similarity index measure (SSIM) between the reconstruction and the ground truth for the four volumes. The ideal data corresponds to the simulation without Doppler broadening, and the Compton shell is considered to has constant thickness.

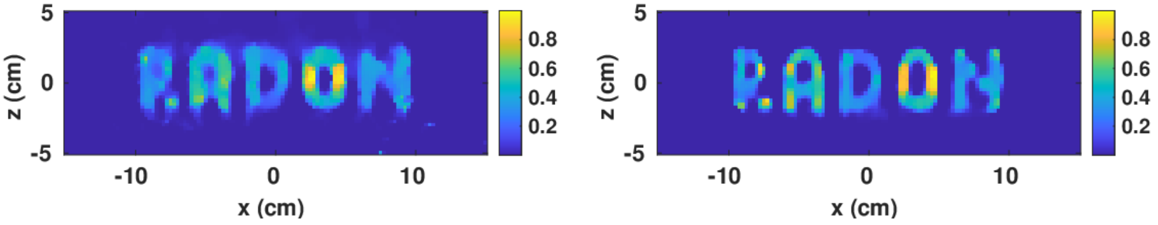

(a) with Doppler broadening (b) without Doppler broadening

Figure 12. Central slices of the reconstructed volume obtained for the non-uniform source when placed perpendicular to the camera. The physics model differ between the two images to include or not Doppler broadening. We used the reconstruction model adapted to each data type. Results are shown after 50 iterations of the TV-MAP-EM algorithm with regularization parameter $\alpha = 5 \times 10^{-6}$. The slices are normalised to their maximum.

Compared to the ideal data projector, the Doppler broadening projector contains a convolution with the kernel h, which becomes wider as we move away from the camera. When Doppler data is reconstructed with the ideal data model, the correction for this convolution is not made and the images are slightly more blurred. This can be seen in figure 13 where we show the image of the vertical source reconstructed with the conical surface model.

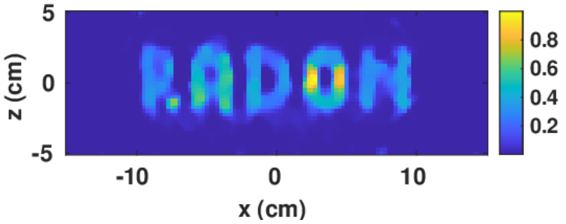

Figure 13. Central slice of the reconstructed volume obtained with the conical surface model applied to Doppler enlarged data. The non-uniform source was placed perpendicular to the camera. TV regularisation was added with parameter $\alpha = 5 \times 10^{-6}$.

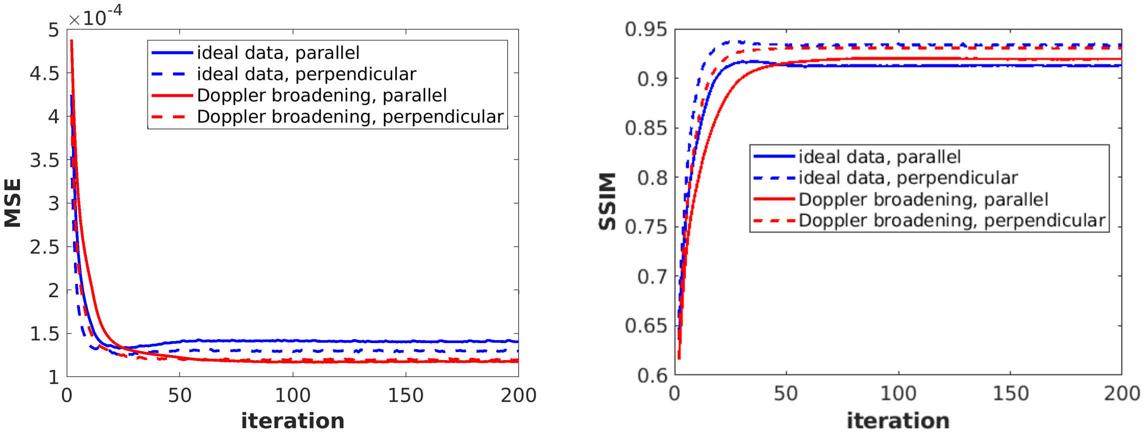

(a) MSE

(b) SSIM

Figure 14. Evolution of the mean square error and of the structural similarity index measure with the number of iterations, for the sources parallel and perpendicular to the camera. Ideal data corresponds to the simulation without Doppler broadening. TV regularization allows the error to decrease to a lower limit and prevents it from rising up significantly after the optimal value is reached. Thanks to the regularization, numerical convergence is largely achieved at 50 iterations for all the reconstructed images and there is no need of an optimal stopping criterion.

4. Discussions

The objective of this paper was to investigate the effect of modeling on the images reconstructed from Compton camera data. We simulated data where the only unknown is the energy dispersion produced by the velocity of the electron on which the γ ray scatters. This process is called Doppler broadening. It causes energy measurement errors that depend on the material and on the energy of the ray. We then calculated the errors that Doppler broadening induce on the Compton angle for a large number of photons. Finally, we fitted a linear combination of two Gaussians to the histogram of errors. The parameters of the fit were included in the reconstruction model as an uncertainty on the measured Compton angle. We compared this model to two other models, one of them consisting to fit only one Gaussian function and the other one being the ideal conical surface model that ignores all uncertainties.

The comparison was first carried with mono-energetic point-like sources. We have been observed in previous tests that when several identical point-like sources are simultaneously placed in the field of view, the reconstructed intensities may not be identical. The PSF is thus varying spatially. Moreover, an elongation of the PSF can be observed in the direction orthogonal to the camera. These artefacts are strongly related to the dimensions of the camera, to the distance from the source to the camera and to the uncertainties on the measurements. We thus take a large camera, relatively ideal data, and we show that modeling can play a decisive role and can alleviate these effects.

Results proved that the mixed Gaussian model is more adapted for image reconstruction than one single Gaussian. The reconstruction results from figures 8 and 10 show that with a more accurate model the elongation artefact in the direction orthogonal to the camera is decreased. The sources were well identified and had similar reconstructed intensities. The PSF should thus be less spatially-variant and radial when a model adapted to the data is used, at least for detectors covering a large field of view at the source position. Besides, the artefacts may also be caused by the mismatch between estimated sensitivity and employed system matrix. For list mode data the sensitivity matrix can only be estimated from Monte Carlo simulation or analytic models, instead of being calculated by summing the system matrix element. More accurate reconstructed images can be expected by finding a compensation between system matrix modeling and estimated sensitivity.

In all simulations we considered that the first interaction took place in the scatterer. In our tests with point-like sources this is true for about 98% of the two-site Compton events. For the remaining 2% of events, the coefficients of our model, fitted for the silicon, are wrong. This strategy could be ameliorated and replaced with a method that can identify the order of interactions with a good probability. Also, considering event-dependent mixture parameters as in [19] is a more costly but potentially more precise alternative.

Compton cameras become interesting for nuclear medicine application above a limit of approximatively 300 keV. Below this limit collimated cameras perform better. As the energy of the photons increases, Doppler broadening decreases and there is lower interest of modeling it. The value we chose in our tests, 511 keV, is slightly above this limit but low enough to justify careful handling of the Doppler effect.

The MLEM algorithm is well-adapted to reconstruct point-like sources. For other geometries smoothing should be introduced in the process, either as a post-processing step or during the iterations. In this work we used TV regularization that is well adapted to our piece-wise constant sources. For smooth intensity distributions, TV regularization will produce cartoon-like images. Compared to the non-regularized MLEM algorithm, total variation regularization allows to accelerate convergence in the sense of the mean squared error and to reduce dependence of the result on the stopping criterion (see figure 14). Figures 11 and 12 show slices reconstructed with the most adapted model and for data simulated with and without Doppler broadening. Figure 13 shows the result of application of the ideal conical surface model to Doppler enlarged data. The result is not very different from the one obtained with the Gaussian mixture model and displayed in figure 12, however the elongation artefacts are slightly more important and creates more ghost activity at the bottom of the source.

5. Conclusions

Elongation of the sources, non uniform intensities and blur were often observed in the direction orthogonal to the camera for Compton camera imaging. We show here that improving modeling of the physical processes during the reconstruction contributes to alleviate these artefacts. This study concentrates on investigating the energy uncertainties caused by Doppler broadening in ideal condition. No errors in the measurement were added and the simulations were carried out with a large field of view, with the simulated source placed close to a large surface camera. The Gaussian mixture model we obtain by fitting the Monte-Carlo simulated ARM allows to strongly improve the spatial uniformity of the reconstructed point spread functions.

We propose a Gaussian mixture fit for the ARM distribution of Monte Carlo simulated data for an ideal Compton camera composed of a scatterer in silicon and an absorber in $LaBr_3$. This model is physically sound and reproduces relatively well the data when only Doppler uncertainties are considered. It allows to strongly improve the spatial uniformity of the reconstructed point spread functions. For realistic data, the detector introduces energy uncertainties and the sequence of interactions has unknown ordering. The fit of a model to the ARM is more difficult in this case and remains an open problem. The choice of the probabilistic distribution that fits Doppler broadened data is just a small step, that at best can give a perfect fit valid only for ideal data. The parameters of the fit seem relatively independent of the angular coverage but strongly depend on the energy of the source and on the material of the detector.

In this study more general uncertainties caused by detector resolution, as well as false coincidences, are leaved out. The Gaussian mixture considered here might be insufficient for realistic data and more complex models or even image-space resolution recovery methods should be employed. Besides, the artefacts on MLEM reconstructed images may also be caused by an mismatch between estimated sensitivity and employed system matrix. Further investigation on the sensitivity calculation, as well as the Monte Carlo based system matrix modeling can be expected. However, we have shown that an accurate acquisition modeling largely improves the quality of the images and such a method could be implemented to deal with other types of uncertainties.

Acknowledgment

The authors acknowledge financial support of the French National Research Agency through the ANR project LABEX PRIMES (ANR-11-IDEX-0007) of Université de Lyon. The authors also acknowledge the anonymous referees for their thoughtful reading of the paper and for their constructive remarks.

References

[1] Schönfelder V, Hirner A, and Schneider K. A telescope for soft gamma ray astronomy. Nuclear Instruments and Methods, 107(2):385–394, 1973.

[2] Todd R, Nightingale J, and Everett D. A proposed γ camera. Nature, 251:132–134, 1974.

[3] Krimmer J, Ley J L, Abellan C, Cachemiche J P, Caponetto L, Chen X, Dahoumane M, Dauvergne D, Freud N, Joly B, Lambert D, Lestand L, Létang J M, Magne M, Mathez H, Maxim V, Montarou G, Morel C, Pinto M, Ray C, Reithinger V, Testa E, and Zoccarato Y. Development of a Compton camera for medical applications based on silicon strip and scintillation detectors. Nuclear Instruments and Methods in Physics Research Section A: Accelerators, Spectrometers, Detectors and Associated Equipment, 787(0):98 – 101, 2015.

[4] Priegnitz M, Barczyk S, Keitz I, Mein S, Stappen FV, Janssens G, Hotoiu L, Smeets J, Fiedler F, Prieels D, et al. Towards clinical application: prompt gamma imaging of passively shaped proton fields with a knife-edge slit camera. Radiotherapy and Oncology, 118:S86–S87, 2016.

[5] Singh M and Doria D. An electronically collimated gamma camera for single photon emission computed tomography. Part II: Image reconstruction and preliminary experimental measurements. Medical physics, 10(4):428–435, 1983.

[6] Takeda S, Odaka H, Ishikawa S, Watanabe S, Aono H, Takahashi T, Kanayama Y, Hiromura M, and Enomoto S. Demonstration of in-vivo multi-probe tracker based on a Si/CdTe semiconductor Compton camera. IEEE Transactions on Nuclear Science, 59(1):70–76, Feb 2012.

[7] Motomura S, Kanayama Y, Hiromura M, Fukuchi T, Ida T, Haba H, Watanabe Y, and Enomoto S. Improved imaging performance of a semiconductor Compton camera GREI makes for a new methodology to integrate bio-metal analysis and molecular imaging technology in living organisms. Journal of Analytical Atomic Spectrometry, 28:934–939, 2013.

[8] Pausch G, Golnik C, Schulz A, and Enghardt W. A novel scheme of Compton imaging for nuclear medicine. In 2016 IEEE Nuclear Science Symposium, Medical Imaging Conference and Room-Temperature Semiconductor Detector Workshop (NSS/MIC/RTSD), pages 1–5, Oct 2016.

[9] Kishimoto A, Kataoka J, Taya T, Tagawa L, Mochizuki S, Ohsuka S, Nagao Y, Kurita K, Yamaguchi M, Kawachi N, Matsunaga K, Ikeda H, Shimosegawa E, and Hatazawa J. First demonstration of multi-color 3-D in vivo imaging using ultra-compact Compton camera. Scientific Reports, 7, 2017.

[10] Fontana M, Dauvergne D, Létang J M, Ley J L, and Testa É. Compton camera study for high efficiency SPECT and benchmark with Anger system. Physics in Medicine & Biology, 62(23):8794, 2017.

[11] Maxim V, Frandes M, and Prost R. Analytical inversion of the Compton transform using the full set of available projections. Inverse Problems, 25(9):1–21, 2009.

[12] Maxim V. Filtered backprojection reconstruction and redundancy in Compton camera imaging. IEEE Transactions on Image Processing, 23(1):332–341, 2013.

[13] Vandenberghe S, Asseler Y D, Van de Walle R, Kauppinen T, Koole M, Bouwens L, Van Laere K, Lemahieu I, and Dierckx R A. Iterative reconstruction algorithms in nuclear medicine. Computerized medical imaging and graphics, 25(2):105–111, 2001.

[14] Zhang B and Zeng G L. Two-dimensional iterative region-of-interest (ROI) reconstruction from truncated projection data. Medical Physics, 34(3):935–944, 2007.

[15] Garduño E and Herman G T. Superiorization of the ML-EM algorithm. IEEE Transactions on Nuclear Science, 61(1):162–172, 2013.

[16] DuMont J W M. Compton modified line structure and its relation to the electron theory of solid bodies. Physical Review, 33(5):643, 1929.

[17] Roland Ribberfors. Relationship of the relativistic Compton cross section to the momentum distribution of bound electron states. Physical Review B, 12(6):2067–2074, 1975.

[18] Ordonez C E, Bolozdynya A, and Chang W. Dependence of angular uncertainties on the energy resolution of Compton cameras. In IEEE Nuclear Science Symposium, volume 2, November 1997.

[19] Ida T, Motomura S, Ueda M, Watanabe Y, and Enomoto S. Accurate modeling of event-by-event backprojection for a germanium semiconductor Compton camera for system response evaluation in the LM-ML-EM image reconstruction method. Japanese Journal of Applied Physics, 58(1):016002, 2018.

[20] Maxim V, Lojacono X, Hilaire E, Krimmer J, Testa E, Dauvergne D, Magnin I, and Prost R. Probabilistic models and numerical calculation of system matrix and sensitivity in list-mode MLEM 3D reconstruction of Compton camera images. Physics in Medicine & Biology, 61(1):243–264, 2016.

[21] Muñoz E, Barrio J, Bernabéu J, Etxebeste A, Lacasta C, Llosá G, Ros A, Roser J, and Oliver J F. Study and comparison of different sensitivity models for a two-plane Compton camera. Physics in Medicine & Biology, 63(13):135004, jun 2018.

[22] Feng Y M, Etxebeste A, Sarrut D, Létang J M, and Maxim V. 3D reconstruction benchmark of a Compton camera against a parallel hole gamma-camera on ideal data. IEEE Transactions on Radiation and Plasma Medical Sciences, 4(4):479–488, 2019.

[23] Wilderman S, Clinthorne N H, Fessler J, Hua C, and Rogers WL. List mode EM reconstruction of Compton scatter camera images in 3D. In 2000 IEEE Nuclear Science Symposium. Conference Record (Cat. No. 00CH37149), volume 2, pages 15–292. IEEE, 2000.

[24] Hilaire E, Sarrut D, Peyrin F, and Maxim V. Proton therapy monotoring by Compton imaging: influence of the large energy spectrum of the prompt-gamma radiation. Phys.Med.Biol.61, 2016.

[25] Sauve A C, Hero A O, Rogers W L, Wilderman S J, and Clinthorne N H. 3D image reconstruction for a Compton SPECT camera model. IEEE Transactions on Nuclear Science, 46(6):2075–2084, Dec 1999.

[26] Seo H, Kim C H, Park J H, Kim J K, Lee J H, Lee C S, and Lee J S. Development of double-scattering-type Compton camera with double-sided silicon strip detectors and NaI (Tl) scintillation detector. Nuclear Instruments and Methods in Physics Research Section A: Accelerators, Spectrometers, Detectors and Associated Equipment, 615(3):333–339, 2010.

[27] Wilderman S J, Fessler J A, Clinthorne N H, LeBlanc J W, and Rogers W L. Improved modeling of system response in list mode EM reconstruction of Compton scatter camera images. IEEE Transactions on Nuclear Science, 48(1):111–116, Feb 2001.

[28] Snyder D L, Miller M I, Thomas L J, and Politte D G. Noise and edge artifacts in maximum-likelihood reconstructions for emission tomography. IEEE Trans. on Medical Imaging, 6(3), 1987.

[29] Stute S and Comtat C. Practical considerations for image-based PSF and blobs reconstruction in PET. Physics in Medicine & Biology, 58(11):3849, 2013.

[30] Sidky E Y, Kao C, and Pan X. Accurate image reconstruction from few-views and limited-angle data in divergent-beam CT. Journal of X-ray Science and Technology, 14(2):119–139, 2006.

[31] Sawatzky A, Brune C, Wubbeling F, Kosters T, Schafers K, and Burger M. Accurate EM-TV algorithm in PET with low SNR. In 2008 IEEE Nuclear Science Symposium Conference Record, pages 5133–5137, Oct 2008.

[32] Maxim V, Feng Y M, Banjak H, and Bretin E. Tomographic reconstruction from Poisson distributed data: a fast and convergent EM-TV dual approach. Technical Report hal-01892281, Oct 2018.

[33] Reader A J, Julyan P J, Williams H, Hastings D L, and Zweit J. EM algorithm system modeling by image-space techniques for pet reconstruction. IEEE Transactions on Nuclear Science, 50(5):1392–1397, 2003.

[34] Kim S, Seo H, Park J, Kim C, Lee C, Lee S, Lee D, and Lee J. Resolution recovery reconstruction for a Compton camera. Physics in Medicine & Biology, 58(9):2823, 2013.

[35] Aprile E, Curioni A, Giboni K, Kobayashi M, Oberlack U G, and Zhang S. Compton imaging of MeV gamma-rays with the liquid xenon gamma-ray imaging telescope (LXeGRIT). Nuclear Instruments

and Methods in Physics Research Section A: Accelerators, Spectrometers, Detectors and Associated Equipment, 593(3):414–425, 2008.

[36] Boggs S E and Jean P. Event reconstruction in high resolution Compton telescopes. Astronomy and Astrophysics Supplement Series, 145(2):311–321, 2000.

[37] Shepp L A and Vardi Y. Maximum likelihood reconstruction for emission tomography. IEEE Transactions on Medical Imaging, 1(2):113–122, 1982.

[38] Lange K and Carson R. EM reconstruction algorithms for emission and transmission tomography. Journal of computer assisted tomography, 8(2):306–316, 1984.

[39] Berger M J and Hubbell J H. Xcom: Photon cross sections on a personal computer. Technical report, National Bureau of Standards, Washington, DC (USA). Center for Radiation, 1987.

[40] Xu D and He Z. Gamma-ray energy-imaging integrated deconvolution. In IEEE Nuclear Science Symposium Conference Record, 2005, volume 2, pages 882–886, Oct 2005.

[41] Hirasawa M and Tomitani T. An analytical image reconstruction algorithm to compensate for scattering angle broadening in Compton cameras. Physics in Medicine & Biology, 48(8):1009, 2003.

[42] Lojacono X, Richard M-H, Ley J-L, Testa E, Ray C, Freud N, Létang JM, Dauvergne D, Maxim V, and Prost R. Low statistics reconstruction of the Compton camera point spread function in 3D prompt-γ imaging of ion beam therapy. IEEE Trans. on Nuclear Science, 60:3355–3363, October 2013.

[43] Wilderman S J, Clinthorne N H, Fessler J A, and Rogers W L. List-mode maximum likelihood reconstruction of Compton scatter camera images in nuclear medicine. In 1998 IEEE Nuclear Science Symposium and Medical Imaging Conference, volume 3, pages 1716–1720, Nov 1998.

[44] Etxebeste A, Dauvergne D, Fontana M, Létang JM, Llosá G, Mu noz E, Oliver JF, Testa É, and Sarrut D. CCMod: a GATE module for Compton camera imaging simulation. Physics in Medicine & Biology, 65(5):055004, 2020.

[45] Brown J M C, Dimmock M R, Gillam J E, and Paganin D M. A low energy bound atomic electron Compton scattering model for Geant4. Nuclear Instruments and Methods in Physics Research Section B: Beam Interactions with Materials and Atoms, 338:77–88, nov 2014.